Influence of WC on third body behaviour during fretting of cold-sprayed Cu-MoS_2-WC composites

Yinyin Zhang[1,2], Sylvie Descartes[2]*, and Richard R. Chromik[1]*

[1]Department of Mining and Materials Engineering, McGill University, 3610 University Street, Montreal, QC, H3A 0C5, Canada

[2]Université de Lyon, CNRS, INSA-Lyon, LaMCoS, UMR5259, 69621 Villeurbanne, France

*Corresponding authors: richard.chromik@mcgill.ca (Richard R. Chromik)

sylvie.descartes@insa-lyon.fr (Sylvie Descartes)

Abstract

Fretting wear behaviour of cold-sprayed Cu-MoS_2 and Cu-MoS_2-WC composites rubbing against AISI 440C steel was studied under gross slip regime. Third body rheology during running-in and steady state was expressed using tribological circuit according to morphology observations on wear scars and transfer materials on the counterfaces. The velocity accommodation mechanisms (VAMs) were therefore identified. Presence of WC particles boosted generation and ejection of large wear particles during running-in and early steady state, yet promoted more stable and lower third body formation and ejection flows over the subsequent test, which led to considerably improved wear resistance. During steady state, the 12 wt.% of WC particles were able to prevent rapid detachment of tribologically transformed structure (TTS) layer and transfer film that was induced by MoS_2. This was believed to be attributed from microwedging and pinning of the WC fragments.

Key words: hard phase reinforced MMCs; fretting wear; third body rheology; tribologically transformed structure (TTS)

1 Introduction

Fretting damage, which commonly occurs in quasi-static loaded assemblies, is defined as damage of contacting surfaces that are subjected to small amplitude oscillatory motions, [1]. Examples were summarized by Berthier et al. in 1989 [2]. Fretting damage triggers failures and causes machine elements to lose functionality, contributing to inefficient operation, increased downtime for repair and eventual need for replacement [2]. Depending on loading conditions, fretting damage takes place by fretting wear or fretting fatigue [2-4]. Fretting wear commonly occurs under gross slip regime while fretting fatigue is often observed at partial slip and mixed regime [1].

In order to protect machine components from fretting damage, surface coatings have been an effective approach, but often with different strategies. For instance, hard films such as TiN and TiC deposited on a high-speed steel yielded negligible wear in gross slip regime [5, 6]. In contrast, soft coatings, namely CuNiIn and MoS_2 [7, 8] , can be applied to reduce shear stress and therefore could potentially improve fretting fatigue resistance particularly when running in partial and mixed regimes [2]. However, hard coatings were vulnerable to fatigue cracking, and the soft coatings were found to be limited in life-time. Self-lubricating metal matrix composites (SLMMCs), which can also be used as coatings, have the lubricant "built-in" and are designed to replenish solid lubricant continuously at the sliding contact, which can help to build up lubricious third bodies [9].

Our previous study on SLMMC coatings of Cu-MoS_2 under gross slip regime demonstrated that presence of MoS_2 facilitated fast development of wear debris bed that separated two first bodies and hence protected them from further wear at a low normal load (i.e. 100 N), while at 150 N normal load, a sharp raise in wear volume took place due to poor bonding between Cu and MoS_2 [10]. This transition from mild wear to severe wear regimes with increasing normal load was commonly observed in SLMMCs [11]. Since impregnation of hard phases such as ceramics to fabricate metal matrix composites or hybrid SLMMCs effectively improves mechanical property of the matrix materials [12, 13], in the present work, a Cu-MoS_2-WC composite was produced and examined under gross slip regime using a normal load of 150 N. The fretting wear behaviour was compared to a Cu-MoS_2 composite to explore the role of WC particles on third body behaviour and wear resistance.

In addition, we expressed the fretting wear behaviour of the above two composites via the tribology circuit, in which flows and rheology of third bodies in the contact were observed to understand better roles of third bodies [4, 14]. As shown in Fig. 1, the tribological circuit depicts third body rheology in an elementary two-dimensional contact. $\mathbf{Q_s}$ represents detachment of first body material to become third bodies; $\mathbf{Q_i}$ is movement of material across the interface; $\mathbf{Q_e}$ is material ejected from the contact; $\mathbf{Q_r}$ is ejected material that is reintroduced to the contact; and $\mathbf{Q_w}$ is material permanently removed from the tribosystem. This concept was firstly introduced by Godet [15] and subsequently developed by Berthier [4, 14]. The tribological circuit has been applied to solid lubricants and metallic materials to describe third body rheology and how it controlled friction and wear behaviour [16, 17].

2 Experimental

2.1 Cold spray deposition of composites

Cu-MoS_2 and Cu-MoS_2-WC composite coatings were deposited onto aluminium alloy (AA6061) substrates using a PCS800 cold spray system (Plasma Giken, Japan). Feedstock powders were prepared by admixing spherical Cu powder (Tekna Advanced Materials Inc., d_{50} = 26 µm) with 5 wt.% of flake-like MoS_2 powder (Climax, d_{50} = 30 µm) for Cu-MoS_2 composite, while for Cu-MoS_2-WC composite, 19 wt.% WC (Tekna Advanced Materials Inc., d_{50} = 30 µm) was added. Other details including carrying gas type (i.e. nitrogen), gas pressure and temperature, spray velocity, gun stand-off distance were presented in a previous work [10]. The substrates were grit-blasted and then preheated up to around 170°C prior to coating deposition by traversing the spray gun slowly (~5 mm/s). over the substrate with the heated gas jet only. The mix was fed at an average rate of around 45 g/min, achieving coatings of roughly 3 mm thick after 3 passes. Deposition efficiency (DE) of each component e.g. MoS_2 was calculated using the MoS_2 remained in the coating divided by MoS_2 sprayed onto the substrate (see equation 1):

$$DE_{MoS2} = \frac{M_{coating} * c_{MoS2}}{M_{sprayed} * C_{MoS2}} = DE_{coating} * \frac{c_{MoS2}}{C_{MoS2}} \quad (1)$$

where $M_{coating}$ is coating mass, c_{MoS2} mass concentration of MoS_2 in the coating, $M_{sprayed}$ is the mass of materials sprayed onto the substrate, C_{MoS2} is the mass fraction of MoS_2 in the feedstock,

$DE_{coating}$ is deposition efficiency of the composite coating. The results are shown in Table 1. Cross sectional micrographs of the two composites (see Fig. 2) were used to examine the distribution of MoS_2 and WC and the concentration of MoS_2 and WC was measured by image analysis. Ten backscattered electron (BSE) images of polished cross sections were randomly taken and analyzed by pixel count. Average MoS_2 content in Cu-MoS_2 is around 1.8 wt.%, while in Cu-MoS_2-WC coating is around 2.2 wt.%, both much less than that in the feedstock. The WC concentration in the coating is around 12 wt.%, slightly lower than that in the feedstock. Hardness ($HV_{0.2}$) of Cu-MoS_2 and Cu-MoS_2 matrix in Cu-MoS_2-WC show similar values of 104 ± 27 $HV_{0.2}$ and 111 ± 24 $HV_{0.2}$, respectively.

Table 1 Deposition efficiency of each component in Cu-MoS_2 and Cu-MoS_2-WC

Coatings	**Deposition efficiency (%)**		
	Cu	MoS_2	WC
Cu-MoS_2	70	25	n/a
Cu-MoS_2-WC	68	27	38

2.2 Fretting wear test

Fretting wear tests were carried out on a custom-built ball-on-plate fretting device at the Laboratoire de Mecanique des Contacts et des Structures (INSA de Lyon, France) in ambient (relative humidity of 30-50%) at room temperature (20-25°C). The upper ball is stationary, yet the lower plate vibrates with a small amplitude of displacement. A stainless steel ball (AISI 440C, Ra = 0.08 µm) with a radius of 50 mm was used as counterface. Prior to fretting wear tests, the composites were mechanically polished using water based 9 and 3 µm diamond suspensions. Fretting wear tests were conducted at a normal load (Fn) of 150 N, an imposed slip amplitude (δ^*) of ± 200 µm, and a frequency of 5 Hz. Those parameters were selected to achieve gross slip condition. The contact condition throughout tests was monitored using a three-dimensional fretting log that plots tangential force (Q) vs. sliding amplitude (δ) and time [1, 18]. In Fig. 3, taking a test of Cu-MoS_2-WC as an example, it experienced a mix regime where both partial slip and occasional gross slip exist at the very beginning, followed by a gross slip regime. In order to examine intermediate states and evolution of interfacial dynamics, tests with cycle numbers of 3,500, 10,000 and 30,000 were conducted.

2.3 Characterization of wear scars and counterfaces

After fretting wear tests, morphology of the wear scars and transfer material on the counterfaces were examined by a scanning electron microscope (SEM) (FEI, Quanta 600, USA) and a confocal non-contact profilometer (Altisurf-500, Altimet, France). Wear rates at 10,000 and 30,000 cycles were calculated using normalized volumetric method, i.e. wear volume, volume below the unworn surfaces of Cu-MoS_2 and Cu-MoS_2-WC, divided by a product of the applied normal load and sliding distance. Counterfaces were not included because no observable wear was measured.

Subsurface microstructure of wear scars was examined by first cutting the 30,000 cycle-wear scars longitude to sliding direction. This was then followed by cold mounting, mechanical grinding and polishing. The surface was finally treated by Ar^+ ion milling to remove a thin layer to eliminate influence of previous mechanical polishing. Electron channelling contrast images (ECCI) [19, 20] were taken using a BSE detector on FEI Inspect 50 to reveal grain and defect contrast, and an annular energy dispersive X-ray (EDX) detector mounted in Hitachi SU-8230 to achieve high resolution elemental distribution maps.

A nanoindenter (Hysitron, Ubi3, USA) equipped with a Berkovich diamond tip was used to measure hardness of the subsurface microstructures of wear scars, AISI 440C counterface, as well as WC particles that were measured from cross section of Cu-MoS_2-WC composite. Indentation was carried out using a load function of 5 s linear loading time to a peak load of 1mN, 2 s holding time at peak load, and 5 s linear unloading time. Hardness values were then obtained using Oliver and Pharr method [21]. Each value reported in the present work was an average of at least 20 indentation tests.

3 Results

3.1 Friction and wear

Average coefficients of friction (CoFs) versus cycle numbers of Cu-MoS_2 and Cu-MoS_2-WC composite coatings are plotted in Fig. 4a. Cu-MoS_2 started with an initial running-in peak of around 0.50 during the first 5300 cycles, then decreased to a steady-state value between 0.4 and 0.45. Cu-MoS_2-WC experienced a slightly longer running-in peak (~ 7600 cycles) with a peak

value of around 0.52, then gradually increased from the end of the peak (i.e. 0.45) to roughly 0.53 and remained the same for the rest of the test. Cu-MoS_2-WC showed considerably more stable friction behavior than Cu-MoS_2 after the running-in peak. It is worth to note that sudden drops and spikes in friction during running-in for both composites was caused by presence of MoS_2, which has been reported in more details in our earlier study [10].

Wear rates of Cu-MoS_2 and Cu-MoS_2-WC coatings were calculated at 10,000 cycles and 30,000 cycles (see Fig. 4b). Cu-MoS_2-WC generated more wear than Cu-MoS_2 during the first 10,000 cycles, then yielded significantly lower wear rate over the steady state.

3.2 Morphology of Cu-MoS_2 and Cu-MoS_2-WC contacts during running-in

Fig. 5 shows the morphology of a Cu-MoS_2 wear scar at 3,500 cycles, which was during the running-in period. Roughly 80% of the contact area was covered by wear debris with varied sizes from less than 1 µm to over 10 µm (see Fig. 5a-b). Particle detachment was initiated by adhesion, as evidenced by smearing-induced tongue-shaped, layered structure on the wear scar surface (see Fig. 5c-d). Cracks that were perpendicular to sliding direction were formed, indicating high stress on the rubbing surface (see Fig. 5d). Ejected wear debris at 3,500 cycles were mostly distributed at two ends of the contact (see Fig. 5e). They were large metallic plates, around 100 - 200 µm in size, and appeared as rough layered structure that was introduced by smearing behaviour (see Fig. 5f). The counterface morphology exhibited initial development of transfer film (see Fig. 6b). The other areas were covered by fine wear debris that was compacted and less than 1 µm in size (see Fig. 6c).

For a Cu-MoS_2-WC wear scar at 3,500 cycles (see Fig. 7a), around 90% of the contact was covered by wear debris, higher than that of the Cu-MoS_2 wear scar (see Fig. 5a). Similar to the Cu-MoS_2 contact, wear debris sizes had a wide size range of around 0.5 µm to 20 µm (see Fig. 7b). At the center of the wear scar, there was a WC particle that was dislodged, leaving a groove behind (see Fig. 7b). Smaller, non-spherical pieces of WC were frequently observed on the wear scar surface (Fig. 7c. These particles could be from the coating itself, which contained a small fraction of WC that had fractured during cold spray. However, as most WC in the coating is spherical, they are most likely from dislodged WC particles that fracture and breakdown with continued fretting. The WC fragments also mix with loose metallic wear debris and embedded locally into metallic

material (Fig. 7d). Evidence of material smearing was also found (Fig. 7d), yet in a much smaller amount comparing to Cu-MoS_2 wear scar at 3,500 cycles. Wear particles that were ejected out of the contact were large metallic debris of a similar size as that observed for Cu-MoS_2 (see Fig. 7e and 5d). The majority of those metallic debris did not contain WC fragments (see Fig. 7f). Fig. 8 shows morphology of the counterface at 3,500 cycles. At the center of the contact, there was a deep groove which was expected to be caused by the pull-out WC particle found on the wear scar. This was evidenced by the morphology that was left by the WC particle (see Fig. 8c). This indicates WC particles were pushed into the counterface material under the current running condition. BSE image of the groove displayed a WC fragment that was embedded. The other areas of the counterface was covered by compacted wear debris with sizes of roughly 1 μm or slightly less (see Fig. 8d), which was similar to that of Cu-MoS_2 counterface (see Fig. 6c).

3.3 Morphology of Cu-MoS_2 and Cu-MoS_2-WC contact during steady state

The contact morphology evolution during steady state was studied for tests stopped at 10,000 cycles and 30,000 cycles. As seen in Fig. 9a and 9b, at 10,000 cycles, around 93% of the wear scar area for Cu-MoS_2 was covered by fine wear debris that was flake-like. Different from observations during the running-in phase, wear debris ejected from the contact at this stage consisted of small wear particles, as shown in Fig. 9c. At 30,000 cycles, the wear scar was almost fully covered by fine flake-like wear debris (see Fig. 9d and 9e). A small area of the wear scar exhibited severe deformation of wear debris (see Fig. 9f).

Viewed by profilometry and SEM, Cu-MoS_2 transfer films on the counterface exhibited formation and detachment of primary prows at both 10,000 and 30,000 cycles. In Fig. 10a, most of the transfer film was less than 20 μm in thickness. Near the center was a large patch of primary prow that was roughly 70 μm thick, 550-700 μm in length and around 350 μm in width. Next to the prow was a detachment event (see Fig. 10b). Rest of the transfer film (around 94%) was fine wear debris on the surface (see Fig. 10c), which was approximately the same coverage of third bodies as that on the wear scar (see Fig. 9a). At 30,000 cycles, the area of the third body was expanded to around 1.8 times of that at 10,000 cycles. Thickness of the transfer film was more uniform and thinner, around 10 μm thick. Close to the center was a prow that was roughly 20 μm in thickness

and about to detach (see Fig. 10e). Rest of the transfer film was powdery, yet more compacted (see Fig. 10f).

For Cu-MoS_2-WC, at 10,000 cycles, around 96% of the contact was covered by wear debris (see Fig. 11a), about the same as that of Cu-MoS_2 at 10,000 cycles. Wear debris were more compacted (see Fig.11b), which were different from the loose flake-like debris observed from Cu-MoS_2 (see Fig. 9b). The areas that were not covered by wear debris exhibited extensive embedding of WC fragments into matrix material (see Fig. 11c). Outside the contact, as shown in Fig. 11d and 11e, a considerable amount of metallic wear debris that contained fine WC fragments were observed. The presence of WC particles seemed to promote second round ejection of metallic debris. Meanwhile, wear debris made of fine wear particles was also formed rapidly at this stage (see Fig. 11f). At 30,000 cycles, the wear scar was fully covered by wear debris that were either very compacted wear debris or loose particles (see Fig. 12). The loose debris were less than 1 μm in size and they did not show flake-like morphology that was observed at the Cu-MoS_2 contact (see Fig. 12c and 9f).

Comparing to transfer film evolution of Cu-MoS_2, Cu-MoS_2-WC transfer films on the counterfaces were more stable from 10,000 cycles to 30,000 cycles in terms of area, thickness, as well as morphology. At 10,000 cycles, it appeared patchy, yet generally continuous, with thickness ranging from 20 - 40 μm without primary prow (see Fig. 13a). A patch that did not contain WC fragments exhibited a gap with the previously transferred material, indicating poor adhesion. However, a patch of material that was distributed by fine WC fragments well adhered to the counterface visually. At 30,000 cycles, area of the transfer film kept constant roughly, and the thickness became more uniform, mostly around 20 μm (see Fig. 13c). Fine wear debris were on the surface of the transfer film (see Fig. 13d).

3.4 Fretting wear modified microstructures and their mechanical property

Fretting wear modified microstructures were observed from cross sections of wear scars after 30,000 cycles. Fig. 14 shows subsurface microstructures of Cu-MoS_2 wear scar. First, vortices consisting of Cu oxides were formed (see Fig. 14a and 14d), which has been observed commonly in metals, soft metals in particular, under tribological loading in ambient [22-24]. Second, tribologically transformed structure (TTS), that was commonly observed underneath topmost

oxide layer [25], was not continuous and it contained mostly ultrafine grains (UFG), as well as some large equiaxed and elongated grains (see Fig. 14b and 14c). At interfaces between layers and between the TTS and third layer of coarse grained (CG) copper, oxygen or MoS_2 were present, according to EDX map (see Fig. 14c and 14d). Thickness of the layers varied from 300 nm to 4 μm. Below the TTS, a layer consisting CG copper extended 30 - 40 μm below the worn surface (see Fig. 14b), which was believed to be driven by dynamic recrystallization [26-28]. The fretting wear modified microstructures (i.e. TTS and CGs) were marked as mechanically affected zone (MAZ), in which the CGs were noted as transition layer that connected the as-sprayed microstructure and the TTS. In Fig. 14c, a grain size gradient from the transition layer to the TTS was indicated by an arrow. Thin lamellae that contained elongated grains could be newly detached microstructure experienced large shear and compression stress. The noncontinuous feature of the TTS indicates it was consumed quickly to create wear particles.

Subsurface microstructures of Cu-MoS_2-WC wear scar at 30,000 cycles are shown in Fig. 15. From top of the worn surface towards first body (i.e. as-sprayed microstructure), there were three layers, including oxides, a continuous TTS layer and a transition layer (see Fig.15a-b). Beneath the topmost oxide layer, there were WC fragments that were also embedded in the TTS. The TTS layer was 5 - 10 μm in thickness and also appeared as layered structure, where the layers had a relatively uniform thickness of 0.7 - 1 μm. In Fig. 15c, a grain size gradient was observed (marked by an arrow), where elongated grains were at the bottom of TTS layer and UFGs on the top. Large equiaxed grains were randomly distributed inside the UFG layer, which was similar to what was observed in the Cu-MoS_2 TTS layer. The transition layer, however, did not exhibit as pronounced grain growth as that in Cu-MoS_2 and the thickness of the transition layer was much thinner, only around 10 μm (see Fig. 15b-c and 14b-c).

Hardness of the fretting wear modified microstructures, measured by nanoindentation, is shown in Table 2. UFGs inside the TTS layer were highly hardened compared to the unworn cold-sprayed Cu where Cu experienced inhomogeneous deformation during cold spray process [20]. However, the transition layer exhibited a significant reduction in hardness. UFGs in the Cu-MoS_2-WC TTS layer showed a little bit higher hardness than that in the Cu-MoS_2 TTS layer. Such microstructural hardening under tribological loading was widely observed in different metals and metal matrix

ceramic composites (MMCs), where participation of ceramic particles in contact promoted higher hardness increase [16, 29].

Table 2 Hardness of fretting wear modified microstructures and unworn metal

Wear tracks	Hardness (GPa)				
	UFGs	Transition layer (CGs)	Unworn Cu 1st body	AISI 440C counterface	WC particle
Cu-MoS_2	3.0 ± 0.4*	1.89 ± 0.22	2.30 ± 0.28	10.6 ± 1.4	na
Cu-MoS_2-WC	3.2 ± 0.3	1.90 ± 0.23	2.40 ± 0.24	10.6 ± 1.4	27.3 ± 1.5

*: the average values and standard deviations were calculated based on 5 data points or less due to small amount of such microstructure.

4 Discussion

Cold-sprayed Cu-MoS_2 and Cu-MoS_2-WC were subjected to fretting wear under gross slip conditions against 440C steel. Based on the results presented in the previous section, the influence of WC on third body behaviour and wear resistance can be described schematically, as shown in Fig. 16. During initial cycles, the ejection of large metallic particles occurred and was similar for both Cu-MoS_2 and Cu-MoS_2-WC composites. This early stage of wear was observed previously for Cu-MoS_2 and is related to particle detachment (source flow) due to MoS_2 at Cu-Cu interfaces [10]. The fact this wear mechanism also occurs for Cu-MoS_2-WC indicates that 12 wt.% WC reinforcement was not in sufficient quantity to cut off this source flow. Detachment of these particles led to a sudden increase in sliding amplitude, as well as abrupt drops in friction during the running-in peaks (see Fig. 3a and 4a). However, when observed the contact, presence of WC particles promoted higher coverage of fine wear debris and minimized adhesion wear mechanism that were observed in Cu-MoS_2 contact and other metal-metal contacts under fretting loading [30, 31]. This could be owing to WC particles and their fragments acting as abrasives in the contact, which could facilitate formation of fine wear debris that was then constrained inside the contact. The velocity accommodation mechanisms (VAMs) during the initial cycles most likely occurred in the first bodies and they were elastic deformation and plastic shearing of the tested composites (see Fig. 5f and 7d), as well as normal breaking of the surface material that served as precursor of particle detachment (see Fig. 5d).

During early stage of steady state (i.e. 10,000 cycles), third bodies developed between the counterfaces and wear scars (see Fig. 16b), and accommodated the velocity difference of the two

first bodies [14]. At the Cu-MoS_2 contact, formation and detachment of primary prows activated internal flow (Q_i). A high volume of third bodies were formed in the contact, which enhanced wear flow (Q_w). This then triggered a high source flow (Q_s) and leading to a high material removal (see Fig. 4b at 10,000 cycles). This could be associated with presence of MoS_2 as it produced poor adhesion between third bodies, leading to detachment from counterface and wear track. As the contact was covered by wear debris, possible VAMs were shearing and/or rolling within the wear debris bed. However, for the Cu-MoS_2-WC contact at early steady state (see Fig. 16b), presence of WC fragments in the contact promoted formation and ejection of large metallic debris that contained WC fragments (see Fig. 11d-e). That suggests a large volume of third bodies were formed (high source flow (Q_s)) and ejected quickly (high wear flow (Q_w)), resulting in a higher material loss than that of Cu-MoS_2. In addition to shearing and/or rolling within the wear debris bed, an important VAM was plastic deformation within the first body (see Fig. 11c). Such process was crucial because stress and strain started to concentrate in the vicinity of WC fragments and form heavily work hardened TTS layer on the wear scar and transfer film on the counterface.

During steady state (i.e. 30,000 cycles), differences for third body behaviour between Cu-MoS_2 and Cu-MoS_2-WC became more pronounced (see Fig. 16c). Due to fast consumption of Cu-MoS_2 TTS layer, as well as formation and detachment of primary prows on the counterface, internal flow (Q_i) was enhanced considerably and a large third body volume in the contact was formed. This led to a high wear flow (Q_w) because trapping was not favoured. This eventually contributed to a high source flow (Q_s). The above third body flows caused a non-continuous TTS layer as well as a high wear rate of Cu-MoS_2 during steady state. Presence of MoS_2 could be the reason of the high volume of the flows. MoS_2 at the bottom of the TTS layer promoted easy detachment of TTS (see Fig. 14c-d), which activated source flow (Q_s) and internal flow (Q_i). Possible VAMs were shearing within wear debris bed and plastic shearing inside the TTS layer. A thick transition layer demonstrated velocity was accommodated by plastic deformation in a large volume of the first body. In addition, the MoS_2 in and beneath the transition layer could accommodate the velocity difference due to its low shear strength.

However, for the Cu-MoS_2-WC contact at steady state (i.e. 30,000 cycles), continuous TTS layer and stable transfer film indicated a small volume of source flow (Q_s) and wear flow (Q_w). Since shear stress and strain were concentrated on the surface, the VAMs in this case were mainly shearing within wear debris bed. Following the method proposed by Descartes et al. [17], who

qualitatively expressed cohesion of third bodies according to their morphology, higher cohesive transfer films and tribofilms were generated during steady state due to the more concentrated stress and strain condition with the presence of WC. This scenario helped to gain significantly higher stability and lower source and wear flows for Cu-MoS_2-WC. This indicates presence of WC particles was capable to prevent formation and ejection of prows that was commonly observed in the Cu-MoS_2 contact. Furthermore, in contrast to a thick transition layer for Cu-MoS_2, a thin transition layer at the Cu-MoS_2-WC wear track demonstrates WC particles constrained plastic deformation on the surface. This suggests during steady-state, the reinforced WC particles in the contact effectively protected the sliding interface from severe wear that was induced by MoS_2 under a high contact pressure.

Causes of the distinction on third body stability observed between Cu-MoS_2 and Cu-MoS_2-WC during steady state were thought to be the following. Firstly, we discussed whether interfacial adhesion of third body materials played a role. It was perhaps not surprising that strong adhesion developed between Cu and AISI 440C steel at initial cycles and then softer Cu was transferred to the harder countersphere to form transfer film (see Fig. 6 and 8). Soria et al. [32] observed drastic transfer from Cu to Incoloy 800 when running at gross slip regime. After the opening cycles, build-up and removal of third bodies actually took place between outer surface of transfer films and wear scar. Since at the current testing environment, there was no evidence showing any chemical interaction occurred between Cu and WC that could lead to higher adhesion, it was reasonable to expect a better bonding should be developed if there was no WC, which did not agree with the present results. Therefore, interfacial adhesion did not explain formation and ejection of primary prows in the Cu-MoS_2 contact versus stable and small volumes of source flow and wear flow in the Cu-MoS_2-WC contact.

Because TTS is the precursor of third bodies, mechanical properties of the TTS layer were believed to be related to the stability of third bodies during steady state [25]. Higher hardness of the Cu-MoS_2-WC TTS layer that was driven by the presence of WC was likely to enhance wear resistance. Shockley et al. [33] observed higher stability of Al-Al_2O_3 third body behaviour than that of Al during sliding wear and attributed it to improved hardness of the highly deformed layer at Al-Al_2O_3 wear tracks. The harder the layer, the more stable the interfacial flows at the sliding contact. The highest hardness of this layer reached in their studies was around 2.5 times as high as that of Al counterpart [33]. Since only slightly higher hardness of the Cu-MoS_2-WC TTS layer was found

in the present work, we believe hardness values alone perhaps could not fully interpret the distinguishable stability of third body flows at the Cu-MoS_2-WC contact. Even so, other mechanical properties such as fracture toughness or ductility of the TTS layer could explain the contrast between the two composites although often it is experimentally challenging due to small amount of TTS material [29]. Those mechanical properties of the TTS layers will probably be presented in the future.

The small WC pieces distributed inside the TTS layer and transfer film likely played a role in keeping them intact and contributed to a low volume of third body in the contact. During formation of transfer films, given that WC fragments were much harder (see Table 2) and sharp (see Fig. 11e), they can serve as microwedges when compressing a piece of detached material that were embedded with WC fragments onto the counterface. Such microwedging of WC could favour generation of the very first layer of transfer film by penetrating relatively softer AISI 440C steel counterface (see Fig. 8c). That was probably why the Cu-MoS_2-WC transfer film was well developed early in the test (i.e. at 10,000 cycles). It also made it easy for detached material to adhere onto the previously deposited transfer film (see Fig. 13b-c). It is worth to note that activation of the wedging effect should also depend on WC sizes, as well as local pressure. Large size of WC (see Fig. 8b) and low spatial contact pressure made it less likely to happen. Moreover, during steady state, the embedded WC pieces could hold the TTS layer and transfer film by pinning. Therefore, they displayed higher stability. The larger WC particles inside the transition layer could also offer pinning effect, which not only carried load but also held the transition layer. In contrast, at the Cu-MoS_2 contact, MoS_2 induced poor adhesion and thus resulted in frequent detachment from the TTS layer and transfer films. This led to high volume of third body flows in the contact and consequently resulted in high wear.

5 Conclusions

Fretting wear behaviour of cold-sprayed Cu-MoS_2 and Cu-MoS_2-WC composites under gross slip regime was examined at a normal load of 150 N, with focus on influence of WC particles on third body rheology and wear resistance. During running-in, even though participation of WC particles and fragments in the contact could not prevent drastic detachment induced by the presence of MoS_2, they promoted a more rapid formation of wear debris bed. The main VAMs took place through elastic and plastic deformation, as well as normal breaking within the first bodies.

During early steady state, WC fragments in the contact caused more material loss. However, during the following test, presence of WC particles constrained velocity accommodation occurred on the top of the wear scar. That contributed to continuous TTS layers and transfer films formed in the contact which favoured more stable and lower volume of third body flows, leading to significantly improved wear resistance of Cu-MoS_2-WC. Presence of the WC fragments inside the TTS and transfer films were believed to be the key to maintain the stable and low source and wear flows by means of microwedging and pinning. In contrast, at the Cu-MoS_2 contact, velocity was accommodated across a large volume of third bodies and first body (i.e. a thick transition layer). The presence of MoS_2 led to frequent detachment from TTS layer and transfer film, which caused consistently high third body flows, resulting in high wear rate.

Acknowledgements

The authors gratefully acknowledge the financial support from Natural Sciences and Engineering Research Council (NSERC) of Canada. They gratefully acknowledge help from Dr. J. Michael Shockley for data analysis, Lionel Lafarge (INSA-Lyon) for the design of the fretting device, Mr. Nicolas Brodusch for technical assistance on scanning electron microscope and Tekna Plasma Systems Inc. and Climax Molybdenum for donation of the powders. The authors acknowledge administrative support from Drs. Phuong Vo, Eric Irissou and Jean-Gabriel Legoux (National Research Council Canada (NRC)) and Stephen Yue (McGill University) and technical support from Mr. Jean Francois Alarie (NRC) at the McGill Aerospace Materials and Alloy Design Center (MAMADC) cold spray facility.

References

1. Vingsbo, O. and S. Söderberg, *On fretting maps.* Wear, 1988. **126**(2): p. 131-147.
2. Berthier, Y., L. Vincent, and M. Godet, *Fretting fatigue and fretting wear.* Tribology international, 1989. **22**(4): p. 235-242.
3. Vincent, L., Y. Berthier, M. Dubourg, and M. Godet, *Mechanics and materials in fretting.* Wear, 1992. **153**(1): p. 135-148.
4. Berthier, Y., L. Vincent, and M. Godet, *Velocity accommodation in fretting.* Wear, 1988. **125**(1): p. 25-38.
5. Fouvry, S. and P. Kapsa, *An energy description of hard coating wear mechanisms.* Surface and Coatings Technology, 2001. **138**(2): p. 141-148.

6. Fouvry, S., T. Liskiewicz, P. Kapsa, S. Hannel, and E. Sauger, *An energy description of wear mechanisms and its applications to oscillating sliding contacts.* Wear, 2003. **255**(1-6): p. 287-298.
7. Fouvry, S. and C. Paulin, *An effective friction energy density approach to predict solid lubricant friction endurance: Application to fretting wear.* Wear, 2014. **319**(1-2): p. 211-226.
8. Mary, C., S. Fouvry, J. Martin, and B. Bonnet, *Pressure and temperature effects on Fretting Wear damage of a Cu–Ni–In plasma coating versus Ti17 titanium alloy contact.* Wear, 2011. **272**(1): p. 18-37.
9. Lansdown, A.R., *Chapter 12 Composites*, in *Tribology Series*, A.R. Lansdown, Editor. 1999, Elsevier. p. 207-244.
10. Zhang, Y., S. Descartes, P. Vo, and R.R. Chromik, *Cold-Sprayed Cu-MoS2 and Its Fretting Wear Behavior.* Journal of Thermal Spray Technology, 2016. **25**(3): p. 473-482.
11. Omrani, E., A.D. Moghadam, P.L. Menezes, and P.K. Rohatgi, *Influences of graphite reinforcement on the tribological properties of self-lubricating aluminum matrix composites for green tribology, sustainability, and energy efficiency—a review.* The International Journal of Advanced Manufacturing Technology, 2016. **83**(1-4): p. 325-346.
12. Rajkumar, K. and S. Aravindan, *Tribological performance of microwave sintered copper–TiC–graphite hybrid composites.* Tribology International, 2011. **44**(4): p. 347-358.
13. Chromik, R.R., S.A. Alidokht, J.M. Shockley, and Y. Zhang, *Tribological Coatings Prepared by Cold Spray*, in *Cold-Spray Coatings*. 2018, Springer. p. 321-348.
14. Berthier, Y., *Experimental evidence for friction and wear modelling.* Wear, 1990. **139**(1): p. 77-92.
15. Godet, M., *The third-body approach: a mechanical view of wear.* Wear, 1984. **100**(1): p. 437-452.
16. Shockley, J.M., S. Descartes, E. Irissou, J.-G. Legoux, and R. Chromik, *Third Body Behavior During Dry Sliding of Cold-Sprayed Al-Al2O3 Composites: In Situ Tribometry and Microanalysis.* Tribology Letters, 2014. **54**(2): p. 191-206.
17. Descartes, S. and Y. Berthier, *Rheology and flows of solid third bodies: background and application to an MoS1. 6 coating.* Wear, 2002. **252**(7-8): p. 546-556.
18. Fouvry, S., P. Kapsa, and L. Vincent, *Analysis of sliding behaviour for fretting loadings: determination of transition criteria.* Wear, 1995. **185**(1): p. 35-46.
19. Joy, D.C., D.E. Newbury, and D.L. Davidson, *Electron channeling patterns in the scanning electron microscope.* Journal of Applied Physics, 1982. **53**(8): p. R81-R122.
20. Zhang, Y., N. Brodusch, S. Descartes, R.R. Chromik, and R. Gauvin, *Microstructure refinement of cold-sprayed copper investigated by electron channeling contrast imaging.* Microscopy and Microanalysis, 2014. **20**(5): p. 1499-1506.
21. Oliver, W.C. and G.M. Pharr, *An improved technique for determining hardness and elastic modulus using load and displacement sensing indentation experiments.* Journal of materials research, 1992. **7**(06): p. 1564-1583.
22. Luo, Z.-P., G.-P. Zhang, and R. Schwaiger, *Microstructural vortex formation during cyclic sliding of Cu/Au multilayers.* Scripta Materialia, 2015. **107**: p. 67-70.
23. Schouwenaars, R., V. Jacobo, and A. Ortiz, *Microstructural aspects of wear in soft tribological alloys.* Wear, 2007. **263**(1): p. 727-735.

24. Liu, Z., C. Patzig, S. Selle, T. Höche, P. Gumbsch, and C. Greiner, *Stages in the tribologically-induced oxidation of high-purity copper.* Scripta Materialia, 2018. **153**: p. 114-117.
25. Zhou, Z., E. Sauger, J. Liu, and L. Vincent, *Nucleation and early growth of tribologically transformed structure (TTS) induced by fretting.* Wear, 1997. **212**(1): p. 50-58.
26. Zhang, Y., H. Niu, L. Zhang, X. Bai, X. Zhang, and P. Zhang, *Grain coarsening behavior in a nanocrystalline copper subjected to sliding friction.* Materials Letters, 2014. **123**: p. 261-264.
27. Yao, B., Z. Han, and K. Lu, *Dry sliding tribological properties and subsurface structure of nanostructured copper at liquid nitrogen temperature.* Wear, 2013. **301**(1): p. 608-614.
28. Zhang, Y., J.M. Shockley, P. Vo, and R.R. Chromik, *Tribological Behavior of a Cold-Sprayed Cu–MoS2 Composite Coating During Dry Sliding Wear.* Tribology Letters, 2016. **62**(1): p. 1-12.
29. Chromik, R.R. and Y. Zhang, *Nanomechanical testing of third bodies.* Current Opinion in Solid State and Materials Science, 2018. **22**(4): p. 142-155.
30. Waterhouse, R.B., *The role of adhesion and delamination in the fretting wear of metallic materials.* Wear, 1977. **45**(3): p. 355-364.
31. Hager, C.H., J. Sanders, S. Sharma, and A. Voevodin, *Gross slip fretting wear of CrCN, TiAlN, Ni, and CuNiIn coatings on Ti6Al4V interfaces.* Wear, 2007. **263**(1): p. 430-443.
32. Soria, S.R., A. Tolley, and A. Yawny, *Characterization of damage and triboparticles resulting from fretting of Incoloy 800 steam generator tubes against different materials.* Wear, 2017. **390-391**: p. 198-208.
33. Shockley, J., S. Descartes, P. Vo, E. Irissou, and R. Chromik, *The influence of Al 2 O 3 particle morphology on the coating formation and dry sliding wear behavior of cold sprayed Al–Al 2 O 3 composites.* Surface and Coatings Technology, 2015. **270**: p. 324-333.

Figure captions:

Fig.1 Tribological circuit describes third body rheology in an elementary two-dimensional contact *dx* [4].

Fig. 2 Cross sectional BSE micrographs of cold sprayed Cu-MoS_2 (a) and Cu-MoS_2-WC (b and c) composites. The dark contrast in (a) and (c) was identified as MoS_2, the bright contrast in (b) and (c) is WC particles.

Fig. 3 Fretting logs of Cu-MoS_2-WC composite coating tested under the following condition: Fn= 150N, δ^*= $\pm$ 200 µm, f = 5 Hz, after 3,500 (a) and 30,000 (b) cycles.

Fig. 4 (a) Average coefficients of friction (CoFs) of Cu-MoS_2, and Cu-MoS_2-WC composites fretting against AISI 440C steel after 30,000 cycles. Double sided arrows mark running-in peaks

of the two tests. (b) Wear rates of Cu-MoS_2 and Cu-MoS_2-WC during 0-10,000 cycles, and 10,000-30,000 cycles.

Fig. 5 Micrographs of Cu-MoS_2 wear scar at 3,500 cycles. (a) overall features; (b) a close view of wear debris inside the contact; (c) a close view of the rectangle in (a), showing an area where adhesion took place; (d) is a close view of cracks that were roughly perpendicular to the sliding direction; (e) morphology of ejected debris; (f) a higher magnification micrograph of the ejected debris. SD indicates the sliding direction.

Fig. 6 SE micrographs of Cu-MoS_2 counterface at 3,500 cycles. (a) overall features; (b) a close view of the rectangle in (a), showing morphology of two-body contact area. SD indicates the sliding direction.

Fig. 7 Micrographs of Cu-MoS_2-WC wear scar at 3,500 cycles. (a) overall features; (b) a close view of the rectangle in (a), exhibiting a pullout of WC; (c) shows crashed WC particles mixed with wear debris; (d) is close view of the rectangle in (a); (e) morphology of ejected large metallic wear debris; (f) a close view of the wear debris. SD indicates the sliding direction.

Fig. 8 Micrographs of Cu-MoS_2-WC counterface at 3,500 cycles. (a) overall features; (b) a close view of the center of the contact, marked as b in (a); (c) a close view of the groove, marked as c in (b); (d) a close view of wear debris inside the contact, marked as d in (a). SD indicates the sliding direction.

Fig. 9 SE micrographs of Cu-MoS_2 wear scar at 10,000 cycles (a-c) and 30,000 cycles (d-f). (a) (d) overall features; (b) a close view of wear debris inside the contact, marked as b in (a); (c) a close view of wear debris outside the contact, marked as c in (a); (e) a close view of wear debris inside the contact, marked as e in (d); (f) a close view of f marked in (d). SD indicates the sliding direction.

Fig. 10 Features of Cu-MoS_2 transfer films at 10,000 cycles (a, b and c) and 30,000 cycles (c, d and e). (a) and (d) are flattened height profiles of the overall features of the transfer films; (b) (e) SE micrographs of the primary prows, that are marked in (a) and (d); (c) (f) SE micrographs of the transfer films at other location. SD indicates the sliding direction.

Fig. 11 Micrographs of Cu-MoS_2-WC wear scar at 10,000 cycles. (a) overall features; (b) a close view of wear debris at the center of the contact, which is marked as b in (a); (c) a close view of c marked in (a); (d) morphology of ejected metallic wear debris marked as d in (a) and (e) is a close view of the debris; (f) SE micrograph of debris made of fine wear particles and marked as f in (a). SD in (a) indicates the sliding direction.

Fig. 12 SE micrographs of Cu-MoS_2-WC wear scar at 30,000 cycles. (a) overall features; (b) a close view of b in (a), showing compacted debris; (c) loose wear debris inside the wear scar, marked as c in (a). SD indicates the sliding direction.

Fig. 13 Features of Cu-MoS_2-WC transfer films at 10,000 cycles (a, b and c) and 30,000 cycles (d and e). (a) and (d) flattened height profiles of the overall features of the transfer films; (b) and (c) BSE micrographs of patches marked in (a); (e) a close view of the rectangle in (d). SD indicates the sliding direction.

Fig. 14 Cross sectional ECCI micrographs of Cu-MoS_2 wear scar at 30,000 cycles. (a) Overall features that were located close to the center of wear scar. The dashed lines indicate interface between the wear scar and mounting epoxy. The dark contrast below was Cu oxides; (b) a patchy TTS layer. The dashed lines indicate interface between as-sprayed microstructure and fretting wear modified microstructure; (c) a detailed image of fretting wear modified microstructure. TTS was a mix of UFG Cu, equiaxed grains, and elongated grains. Below TTS were CG Cu, also marked as DRX layer in (b), TTS layer exhibited as layered structure and a grain size gradient; (d) EDX map of (c), showing elemental composition distributions of O, Cu, and Mo. SD indicates sliding direction.

Fig. 15 Cross sectional ECCI micrographs of Cu-MoS_2-WC wear scar at 30,000 cycles. (a) Overall features that were located close to the center of wear scar. The dashed lines indicate interface between the wear scar and mounting epoxy. The dark contrast below the dashed lines was Cu oxides; (b) a close view of fretting wear modified microstructure that includes TTS and DRX layers. Below the dashed lines was as-sprayed microstructure; (c) a detailed image of TTS microstructure. It is a mix of ultrafine grained Cu (UFG), equiaxed grains, and elongated grains. It appeared as layered feature and a grain size gradient was marked from the DRX layer to TTS layer. SD indicates sliding direction.

Fig. 16 Schematics of third body rheology in the fretting contact of Cu-MoS_2 (left) and Cu-MoS_2-WC (right) fretting against AISI 440C at different stages of testing. (a) high source flow (Q_s) and wear flow (Q_w) due to detachment and ejection of large metallic debris during the initial cycles; (b) early steady state: for Cu-MoS_2, detachment and ejection of primary prows led to high source flow (Q_s), activated internal flow (Q_i), and high wear flow (Q_w); for Cu-MoS_2-WC, presence of WC fragments resulted in formation and ejection of large debris containing small WC fragments, i.e. high volume of source (Q_s) and wear (Q_w) flows, as well as activated internal flow (Q_i); (c) during steady state, frequent detachment of TTS layer and transfer film resulted in high source flow (Q_s), activated internal flow (Q_i) and high wear (Q_w) flows for Cu-MoS_2, while stable TTS and transfer film rendered activated source flow (Q_i), yet much lower source (Q_s) and wear (Q_w) flows for Cu-MoS_2-WC. The amount of Q_s and Q_w are indicated by the thickness of arrows. The number of the arrows underneath Q_s marked volume of the third body.

Fig. 1

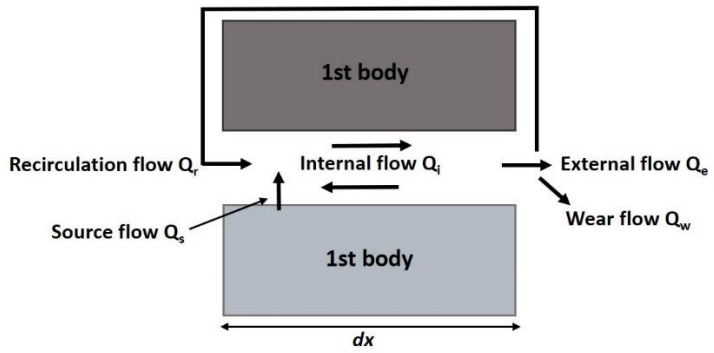

Fig. 2

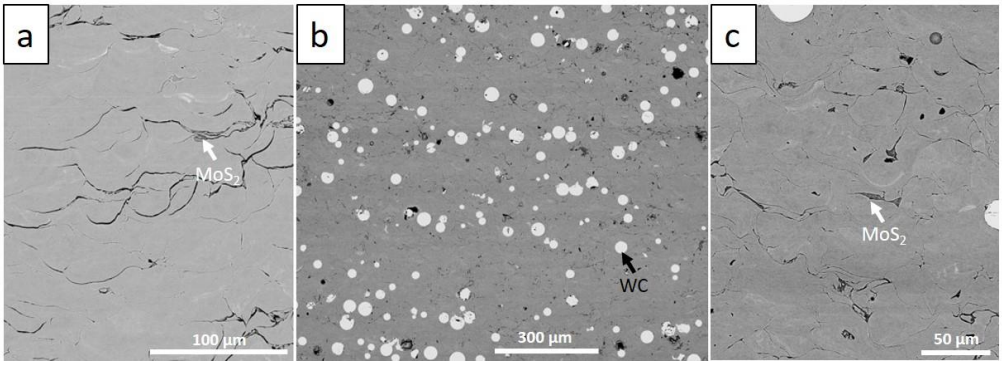

Fig. 3

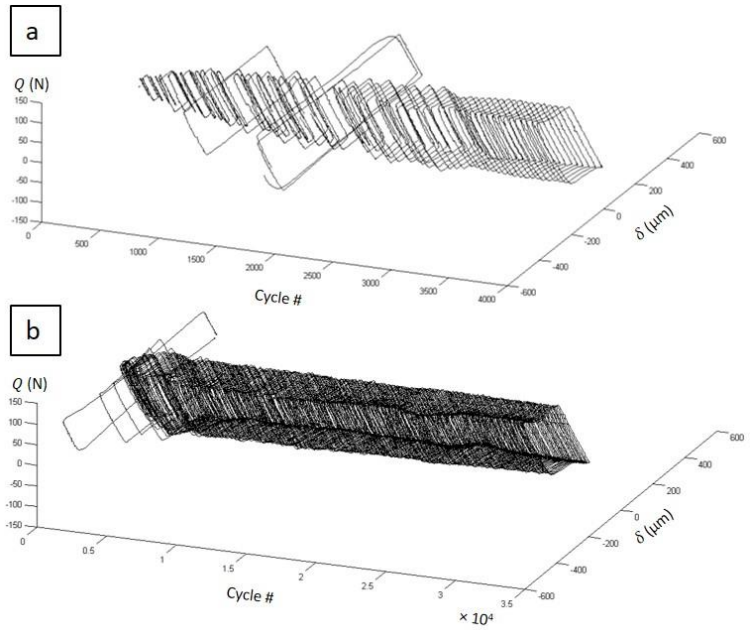
a
Q (N)
Cycle #
δ (μm)
b
Q (N)
Cycle #
× 10⁴
δ (μm)

Fig. 4

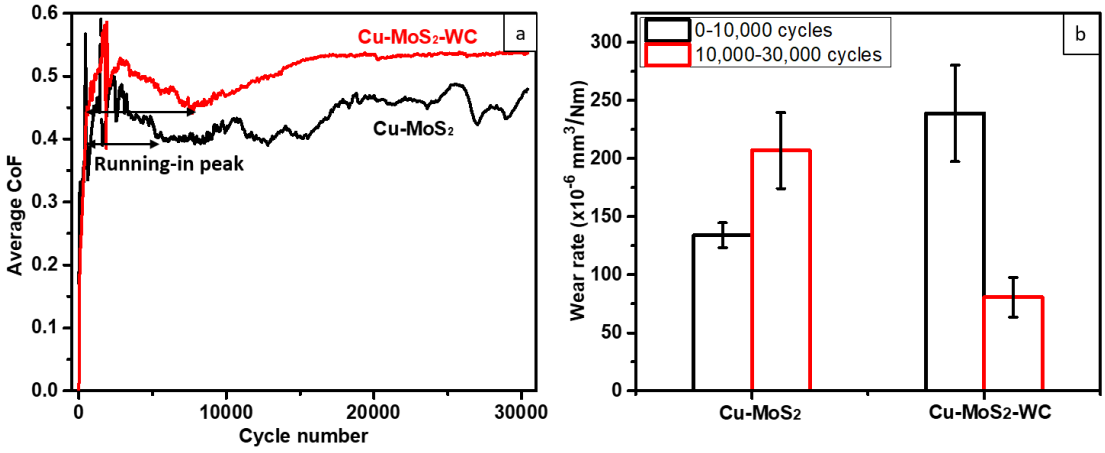
a
Cu-MoS₂-WC
Cu-MoS₂
Running-in peak
Average CoF
Cycle number
b
0-10,000 cycles
10,000-30,000 cycles
Wear rate (x10⁻⁶ mm³/Nm)
Cu-MoS2
Cu-MoS2-WC

Fig. 5

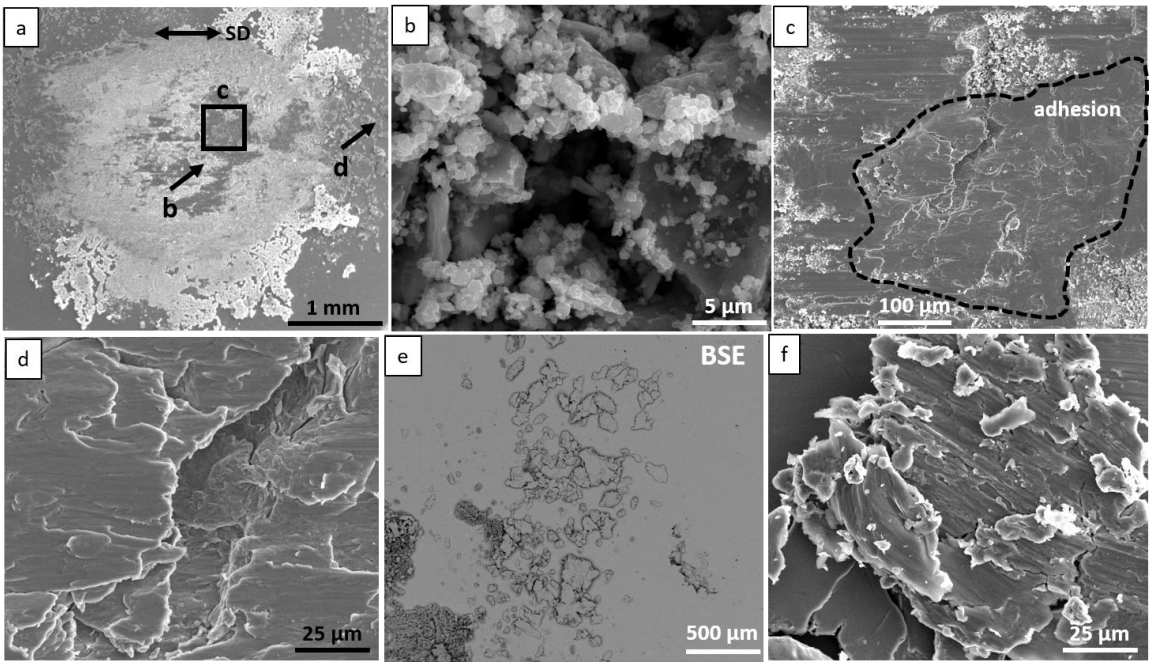
a
SD
c
b
d
1 mm
b
5 µm
c
adhesion
100 µm
d
25 µm
e
BSE
500 µm
f
25 µm

Fig. 6

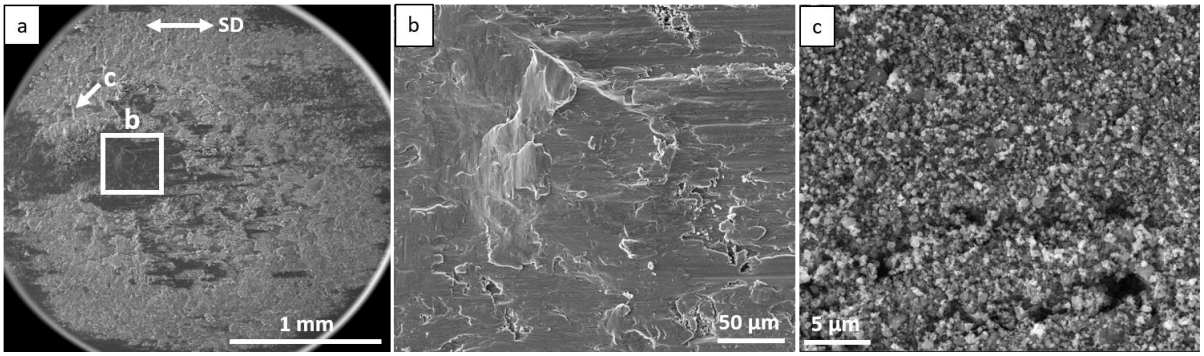
a
SD
c
b
1 mm
b
50 µm
c
5 µm

Fig. 7

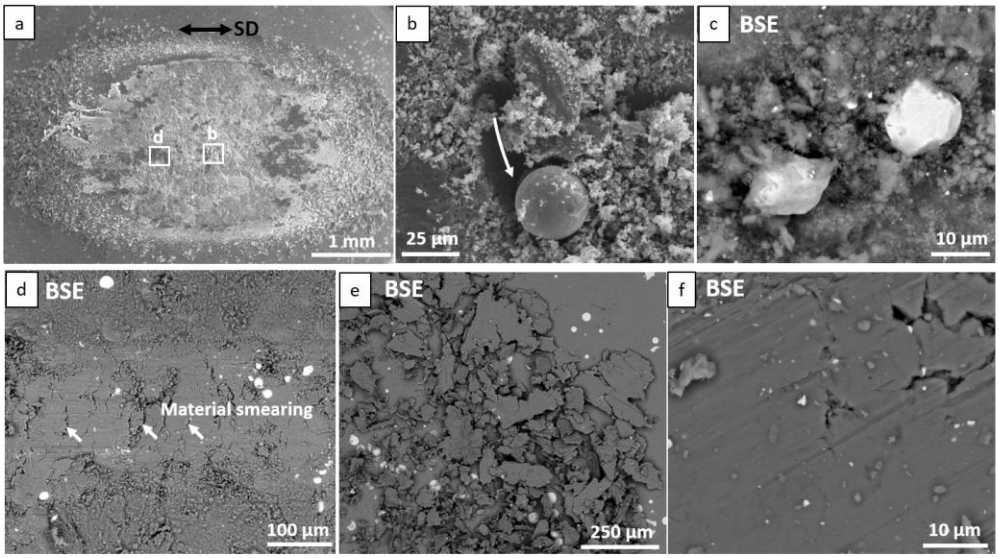
a
SD
d
b
1 mm
b
25 µm
c
BSE
10 µm
d
BSE
Material smearing
100 µm
e
BSE
250 µm
f
BSE
10 µm

Fig. 8

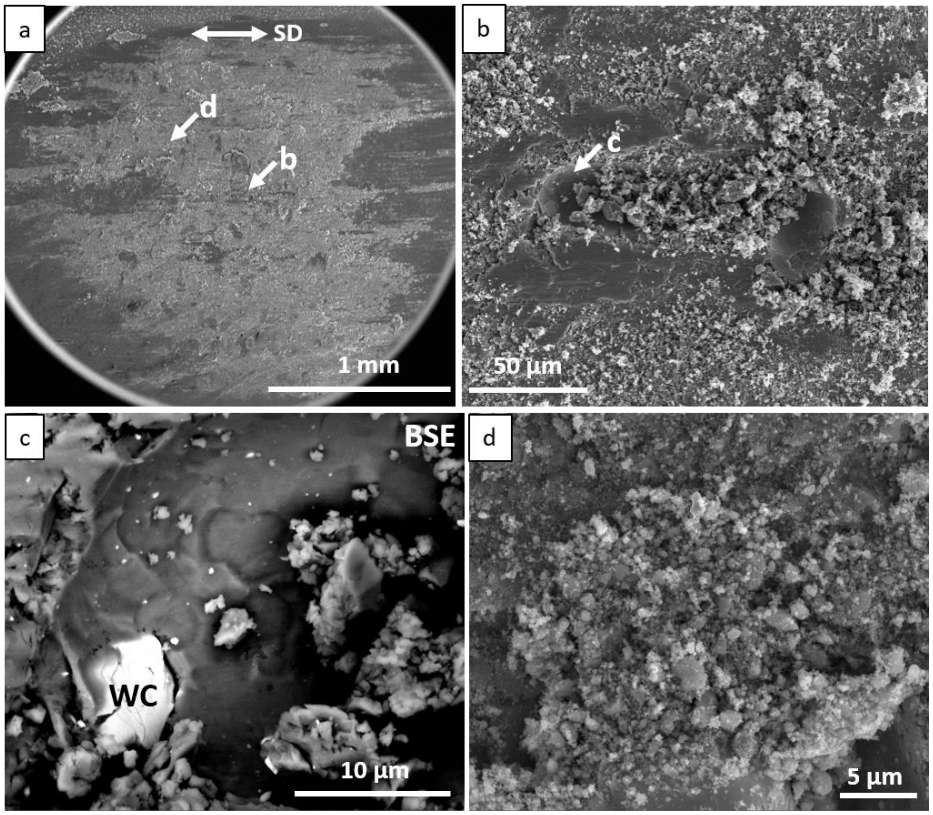
a
SD
d
b
1 mm
b
c
50 µm
c
BSE
WC
10 µm
d
5 µm

Fig. 9

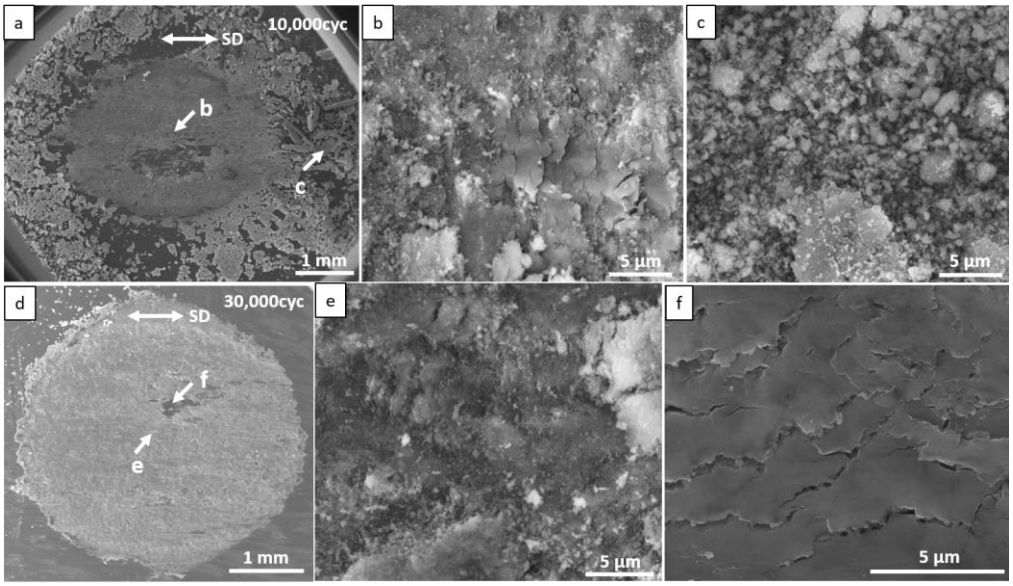
a
10,000cyc
SD
b
c
1 mm
b
5 µm
c
5 µm
d
30,000cyc
SD
f
e
1 mm
e
5 µm
f
5 µm

Fig. 10

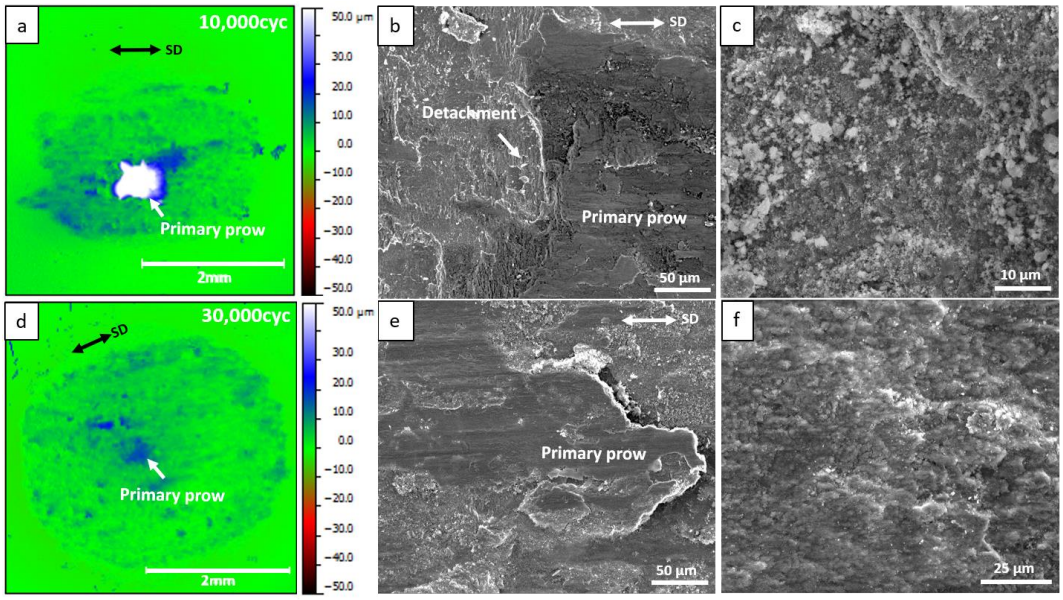
a
10,000cyc
SD
Primary prow
2mm
50.0 µm
30.0
20.0
10.0
0.0
-10.0
-20.0
-30.0
-40.0
-50.0
b
SD
Detachment
Primary prow
50 µm
c
10 µm
d
30,000cyc
SD
Primary prow
2mm
e
SD
Primary prow
50 µm
f
25 µm

Fig. 11

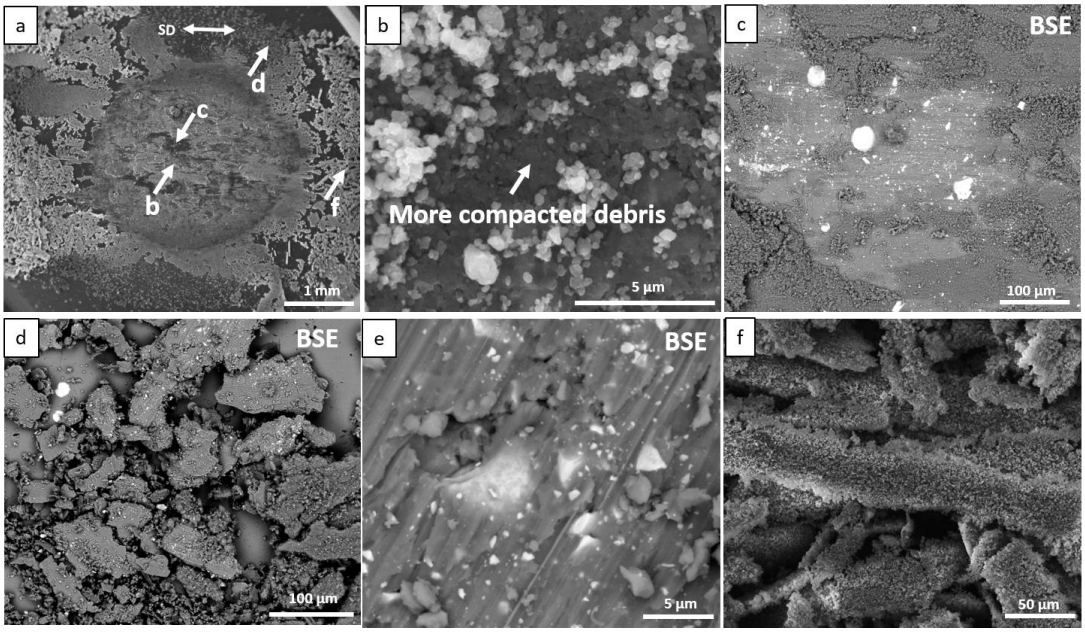
a
SD
d
c
b
f
1 mm
b
More compacted debris
5 µm
c
BSE
100 µm
d
BSE
100 µm
e
BSE
5 µm
f
50 µm

Fig. 12

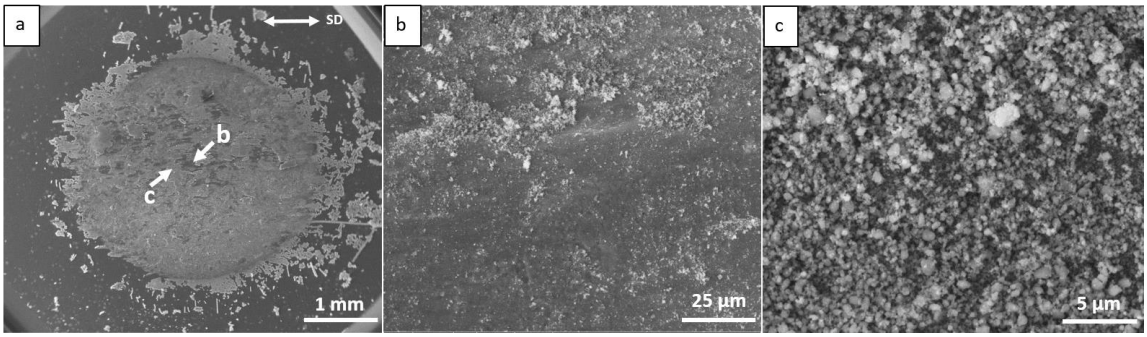
a
SD
b
c
1 mm
b
25 µm
c
5 µm

Fig. 13

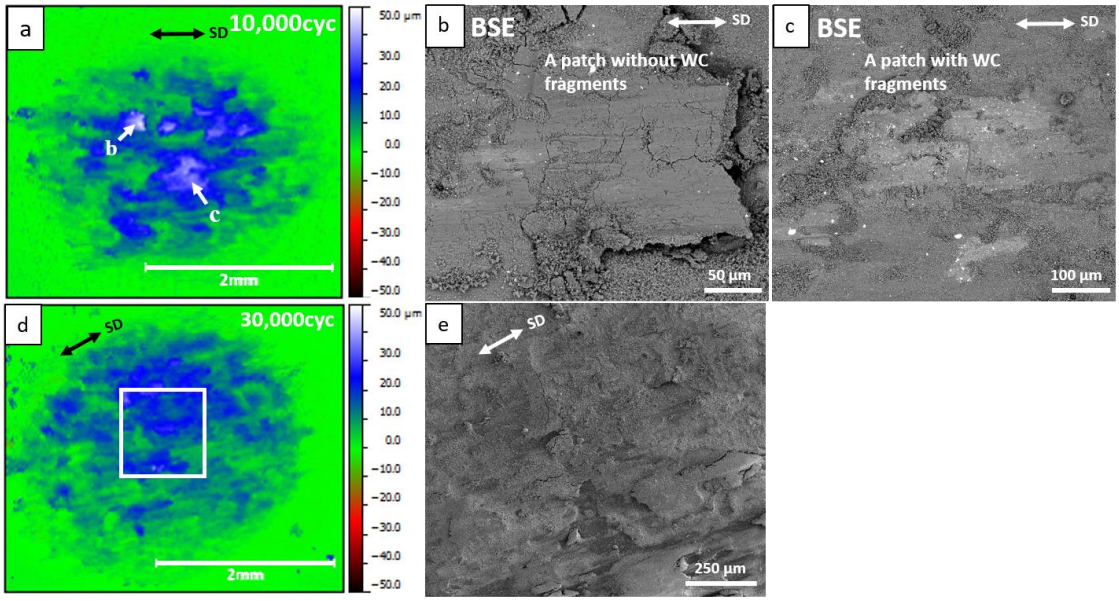
a
SD
10,000cyc
b
c
2mm
50.0 µm
30.0
20.0
10.0
0.0
−10.0
−20.0
−30.0
−40.0
−50.0
b
BSE
SD
A patch without WC fragments
50 µm
c
BSE
SD
A patch with WC fragments
100 µm
d
SD
30,000cyc
2mm
e
SD
250 µm

Fig. 14

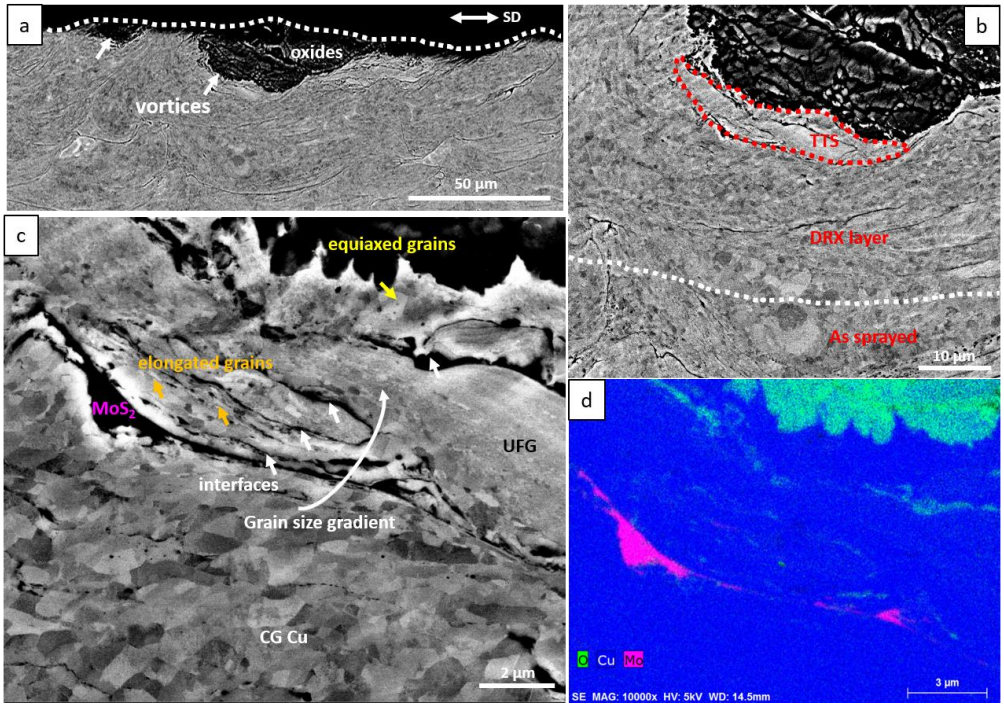
a
SD
oxides
vortices
50 µm
b
TTS
DRX layer
As sprayed
10 µm
c
equiaxed grains
elongated grains
MoS2
UFG
interfaces
Grain size gradient
CG Cu
2 µm
d
Cu
Mo
SE MAG: 10000x HV: 5kV WD: 14.5mm
3 µm

Fig. 15

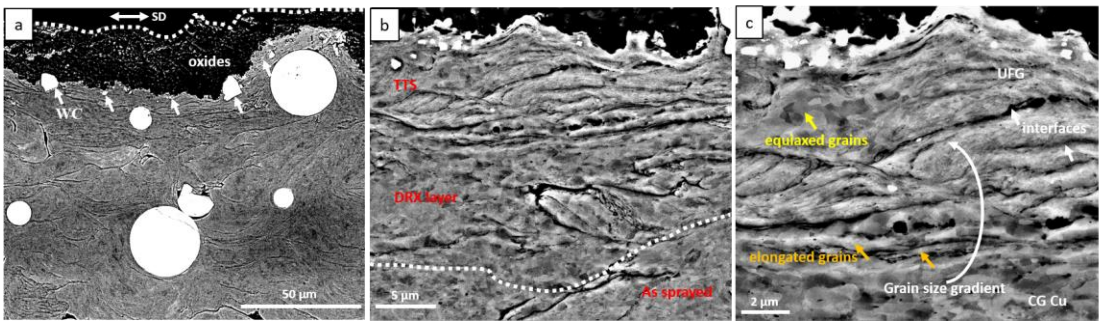
a
SD
oxides
WC
50 μm
b
TTS
DRX layer
As sprayed
5 μm
c
UFG
interfaces
equiaxed grains
elongated grains
Grain size gradient
CG Cu
2 μm

Fig. 16

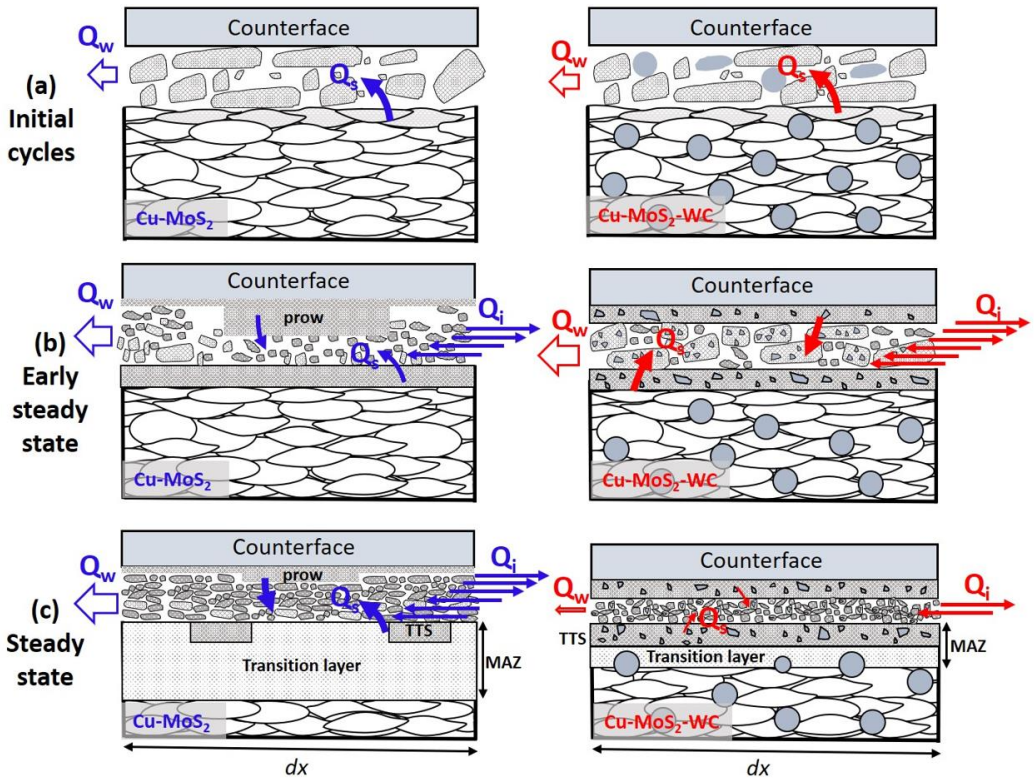
(a)
Initial
cycles
Counterface
Q_w
Q_s
Cu-MoS$_2$
Cu-MoS$_2$-WC
(b)
Early
steady
state
prow
Q_i
(c)
Steady
state
TTS
Transition layer
MAZ
dx